THEORY OF SOFT ELECTROMAGNETIC EMISSION IN HEAVY-ION COLLISIONS*

Ralf Rapp

Cyclotron Institute and Department of Physics and Astronomy
Texas A&M University, College Station, TX 77843–3366, USA

(Received October 19, 2011)

A status report of utilizing soft electromagnetic radiation (aka thermal photons and dileptons) in the diagnosis of strongly interacting matter in ultrarelativistic heavy-ion collisions is given. After briefly elaborating on relations of the electromagnetic spectral function to chiral symmetry restoration and the transition from hadron to quark degrees of freedom, various calculations of electromagnetic emission rates in the hadronic and quark-gluon plasma phases of QCD matter are discussed. This, in particular, includes insights from recent thermal lattice QCD computations. Applications to dilepton and photon spectra in heavy-ion collisions highlight their role as a spectro-, thermo-, baro- and chrono-meter of extraordinary precision.

DOI:10.5506/APhysPolB.42.2823
PACS numbers: 12.38.Mh, 21.65.Jk, 25.75.Cj, 25.75.Nq

1. Introduction

Collisions of heavy nuclei at (ultra-) relativistic energies provide the fascinating opportunity to recreate blobs of strongly interacting matter which last existed naturally almost 14 billion years ago, for a few microseconds after the Big Bang. They are furthermore the only means by which the bulk properties of a nonabelian gauge theory can be compared to experiment. This is particularly important in a situation where the coupling strength is not small, implying nonperturbative and collective phenomena which can only be unraveled in close collaboration between experiment and theory.

Over the last twenty years or so, ultrarelativistic heavy-ion collisions (URHICs) at various laboratories around the world have demonstrated that systematic studies over a large region of the QCD phase diagram are

* Presented at the LI Cracow School of Theoretical Physics "Soft Side of the LHC", Zakopane, Poland, June 11–19, 2011.

possible, *cf.* left panel of Fig. 1. For example, the measured hadron abundances can be well explained by a chemically equilibrated hadron-resonance gas including strange particles (contrary to p–p collisions) [1], and the transverse-momentum (p_t) spectra of hadrons can be well described by an explosive blast-wave source with common temperature and collective "flow" velocity in excess of half the speed of light. The observed azimuthal asymmetries in the p_t spectra in noncentral collisions (the so-called elliptic flow, v_2) can be well accounted for through the pressure gradients as obtained from a locally equilibrated medium driven by hydrodynamic expansion [3]. However, hadronic observables ultimately emanate from the "freezeout" configuration of the fireball (typically at a temperature of $T_{\rm fo} \simeq 100$ MeV), and thus do not provide information on the microscopic structure and interactions of medium.

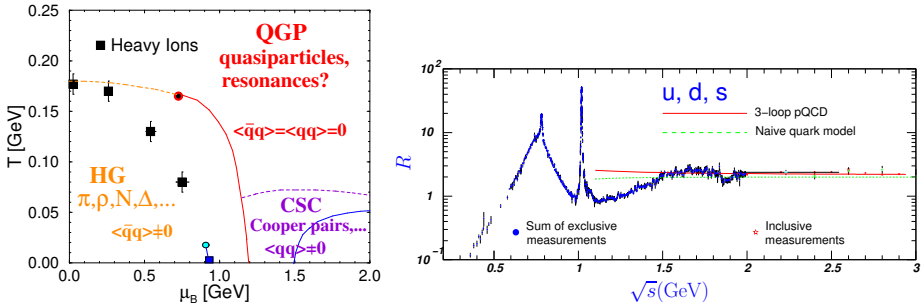


Fig. 1. Left panel: schematic phase diagram of strong-interaction matter, indicating a cross-over transition (dashed line) at large temperature T, and small baryon chemical potential, μ_B, and a first order transition into a color-superconductor (CSC) at small T and large μ_B (solid line). The "data points" represent (μ_B, T) values extracted from ratios of different hadron species employing a thermal hadron-resonance-gas model [1]. Right panel: EM spectral function in vacuum as measured by the R-ratio in e^+e^- annihilation into hadrons (figure taken from Ref. [2]). The EM spectral function is the only one whose medium modifications are directly accessible in heavy-ion collisions, through dilepton invariant-mass spectra.

Electromagnetic (EM) observables, photons and dileptons, are special (see Refs. [4, 5] for recent reviews). Their interaction rate in the strongly interacting medium is small enough for them to escape the interior of the fireball unaffected, but large enough to be produced in measurable quantities. The radiation of photons from a thermalized fireball has been long recognized as a powerful thermometer. The emission of virtual photons (aka dileptons, e^+e^- or $\mu^+\mu^-$) carries additional information in terms of their invariant mass, $M = (q_0^2 - \vec{q}^2)^{1/2}$. In fact, dilepton invariant-mass spectra are the only observable which gives direct access to the in-medium modifica-

tion of a hadronic spectral function (strong decays like $\Delta \to \pi N$ or $\rho \to \pi\pi$ suffer from final state absorption and are largely emanating from the freeze-out process of the collision). This is evident from the 8-differential thermal production rate,

$$\frac{dN_{ee}}{d^4x d^4q} = -\frac{\alpha_{\rm EM}^2}{\pi^3 M^2}\; f^B(q_0;T)\; {\rm Im}\Pi_{\rm EM}(M,q;\mu_B,T)\,, \tag{1}$$

which only depends on the in-medium spectral function, $\mathrm{Im}\,\Pi_{\rm EM}$, its thermal weight in terms of the Bose–Einstein distribution, f^B, and a free virtual-photon propagator, $1/M^2$. A clean temperature measurement becomes possible if $\mathrm{Im}\,\Pi_{\rm EM}$ is reliably known, which is usually the case for large M^2 where temperature corrections can be assessed perturbatively (in principle this also applies for photons at large $q_0^2 = q^2$, but the leading term is already nontrivial in the strong coupling, *i.e.*, $\mathcal{O}(\alpha_{\rm s}T^2)$, while for dileptons it is $\mathcal{O}(1)$). However, the physics accessible through $\mathrm{Im}\,\Pi_{\rm EM}$ is much richer. In the vacuum, the latter is accurately known from the inverse process of e^+e^- annihilation into hadrons, as displayed in the right panel of Fig. 1 in terms of the famous ratio $R = \sigma(e^+e^- \to \text{hadrons})/\sigma(e^+e^- \to \mu^+\mu^-) \propto \mathrm{Im}\Pi_{\rm EM}^{\rm vac}/M^2$. Its medium modifications encode a wide variety of properties of the strongly interacting medium. For example, transport coefficients can be extracted by the space-like and time-like limits of vanishing energy and momentum, corresponding to the EM susceptibility and conductivity, respectively, of the medium. A more ambitious goal is to systematically map out how the hadronic degrees of freedom, represented by the ρ, ω and ϕ resonance peaks, are affected across the QCD phase diagram and in this way reflect its structure. In particular, one would like to find out how the nonperturbatively generated mass of the vector mesons dissolves and how they ultimately yield to a spectral function of weakly correlated quarks at high temperatures, signaling deconfinement. Note that light vector mesons (especially the ρ) may well serve as a prototype hadronic resonance (it is neither a Goldstone boson nor a heavy-quark state) in the sense that their fate in hot/dense matter is shared by a large set of resonances. A hadron-resonance gas is known to give a good approximation of the QCD partition function until close to the phase transition [6].

Mass de-generation and deconfinement are closely related to the fate of the QCD condensates in the medium. Figure 2 shows recent results of thermal lattice QCD for order parameters of the corresponding QCD phase transition(s) [7]. These calculations are carried out for $N_f = 2 + 1$-flavor QCD with realistic light quark masses and clearly demonstrate the cross-over of the transition from a chirally broken hadronic phase to chirally restored partonic matter. It is rather intriguing, though, that the inflection points of these quantities, usually associated with the pseudo-critical

temperature, seem to be separated by about 20 MeV, *i.e.*, $T_c^{\chi} \simeq 150$ MeV and $T_c^{\rm conf} \simeq 170$ MeV for chiral restoration and deconfinement, respectively. Even without the notion of a pseudo-critical temperature, which is not unambiguous, it is still remarkable that at, say, $T \simeq 160$ MeV the Polyakov loop has risen by merely $\sim 10\%$ toward its asymptotic value while the chiral condensate has already dropped to below 50%. This is suggestive for a medium in which chiral symmetry is largely restored but hadrons are still prevalent degrees of freedom (not unlike the "quarkyonic phase" conjectured to exist in the moderate-μ_B region of the QCD phase diagram [9]). This would furthermore imply that hadronic degrees of freedom are the adequate basis to address mechanisms of chiral restoration. Partial chiral restoration in the hadronic phase is very encouraging from an experimental point of view, as it turns out that thermal dilepton emission in the low-mass region (LMR, $M \leq 1$ GeV) is dominated by the contribution from hot and dense matter at temperatures $T \simeq 150$–200 MeV (this follows from the interplay of the increasing 3-volume and the decreasing thermal Bose factor in the space-time integrated spectral yield, see Sec. 3.1 below) [10].

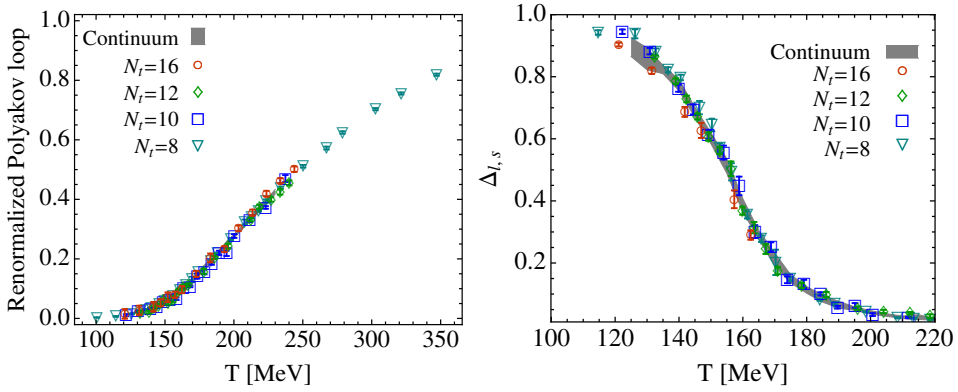


Fig. 2. Results of lattice-QCD computations [7] for the renormalized Polyakov loop (left) and for the "strangeness-subtracted" chiral condensate normalized to its vacuum value, $\langle\bar{q}q\rangle(T)/\langle\bar{q}q\rangle(0)$ (right). Both quantities are order parameters of the QCD phase transition, the former associated with quark deconfinement in the limit of large quark masses and the latter with chiral symmetry restoration for $m_q \to 0$. The computations are carried out with realistic quark masses for $N_f = 2+1$ flavors with the gray band indicating the extrapolated continuum limit. Figures are taken from Ref. [7,8].

The manifestation of the Spontaneous Breaking of Chiral Symmetry (SBCS) in the vacuum EM spectral function becomes apparent upon decomposing it into good isospin states. The dominant contribution arises from the isovector channel ($I = 1$) which in the LMR is essentially saturated by the ρ meson (the contribution of the isoscalar–vector (ω) channel to $\Pi_{\rm EM}$ is down by a factor of ~ 10). The Weinberg sum rules [11,12] relate moments of the isovector–vector and –axialvector spectral functions to order parameters of SBCS,

$$f_n = -\int_0^\infty \frac{ds}{\pi}\, s^n\ \left[{\rm Im}\Pi_{\rm V}(s) - {\rm Im}\Pi_{\rm A}(s)\right]\ . \tag{2}$$

Both spectral functions have been accurately measured in vacuum via hadronic decays of the τ lepton at LEP [13, 14] (see Fig. 3) and constitute one of the best experimental evidences for SBCS. For example, for $n = -1$, one has $f_{-1} = f_\pi^2$, where $f_\pi = 93$ MeV is the pion decay constant (or pion "polestrength"). Recalling the Gellmann–Oakes–Renner relation, $f_\pi^2 m_\pi^2 = -m_q\langle 0|\bar{q}q|0\rangle$, one recognizes the close relation between scalar quark condensate, Goldstone bosons and the isovector axial-/vector spectral functions (the explicit chiral breaking is signified by the small current quark mass, $m_q \simeq 5$ MeV, and the pion mass). The Weinberg sum rules, which remain valid in the medium, exhibit the important role of the axialvector spectral function in the search for chiral restoration from dilepton data: the vector spectral function degenerates with its chiral partner, the axialvector, in the chirally restored phase. Similar to the vector channel, the nonperturbative

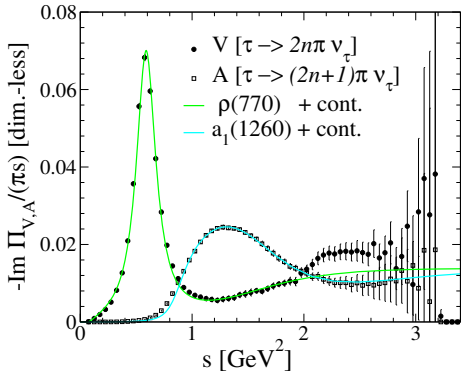


Fig. 3. Vacuum spectral functions of the vector and axialvector currents as measured in hadronic τ decays into Goldstone bosons [13, 14]. The lines are model calculations using ρ and a_1 dominance with smoothly onsetting multi-pion continua.

part of the axialvector channel is dominated by a resonance, the $a_1(1260)$. At higher masses, $M > 1.5$ GeV, one expects from perturbation theory that the axialvector also merges into a continuum which coincides with the vector channel. Another example of relating QCD condensates to empirical spectral functions are QCD sum rules.

The remainder of this article is organized as follows. In Sec. 2 we introduce the vector-current correlator in strongly interacting matter and recall its noninteracting and vacuum limits (Sec. 2.1), review calculations of its spectral function in hadronic (Sec. 2.2) and partonic media including recent results from thermal lattice QCD (Sec. 2.3), and discuss the corresponding thermal production rates of dileptons and photons (Sec. 2.4). In Sec. 3 we turn to the quantitative analysis of EM emission spectra in URHICs, beginning with descriptions of the space-time evolution of the medium over which the rates need to be integrated (Sec. 3.1). Theoretical calculations of EM spectra in URHICs will be compared to experiment to extract information on medium effects of the spectral function, the time duration of emission (spectro- and chrono-meter, Sec. 3.2) and temperature and collective properties of the expanding fireball (thermo- and baro-meter, Sec. 3.3). We conclude in Sec. 4.

2. Vector-current correlator in medium

In this section the central role is played by the hadronic correlation function of two electromagnetic currents defined as

$$\Pi^{\mu\nu}_{\rm EM}(q) = -i \int d^4x \; {\rm e}^{iqx} \; \Theta(x_0) \left\langle \left[j^\mu_{\rm EM}(x), j^\nu_{\rm EM}(0) \right] \right\rangle_T \; , \tag{3}$$

where $\langle \ldots \rangle_T$ denotes the expectation value at finite temperature (giving rise to a retarded spectral function). In a partonic basis, corresponding to the elementary degrees of freedom in the QCD Lagrangian, the EM current takes the form

$$j^\mu_{\rm EM} = \tfrac{2}{3} \bar{u} \gamma^\mu u - \tfrac{1}{3} \bar{d} \gamma^\mu d - \tfrac{1}{3} \bar{s} \gamma^\mu s \, , \tag{4}$$

where we constrain ourselves to the 3 light flavors up, down and strange. The EM current in quark basis, Eq. (4), can be rearranged into good isospin states which naturally leads to the hadronic basis according to

$$\begin{aligned} j^\mu_{\rm EM} &= \tfrac{1}{2} (\bar{u} \gamma^\mu u - \bar{d} \gamma^\mu d) + \tfrac{1}{6} (\bar{u} \gamma^\mu u + \bar{d} \gamma^\mu d) - \tfrac{1}{3} \bar{s} \gamma^\mu s \\ &= \tfrac{1}{\sqrt{2}} j^\mu_\rho + \tfrac{1}{3\sqrt{2}} j^\mu_\omega - \tfrac{1}{3} j^\mu_\phi \end{aligned} \tag{5}$$

with the properly normalized hadronic currents, j^μ_v ($v = \rho, \, \omega, \, \phi$). Invoking the Vector-Dominance Model (VDM) characterized by the field–current

identity $j_v^\mu = v^\mu\, m_v^2/g_v$, the hadronic currents are saturated by the light vector mesons and the pertinent current–current correlator turns into a vector–meson propagator, D_v.

2.1. EM spectral function in vacuum and thermal emission rates

The imaginary part of the EM current–current correlator is the EM spectral function. In the vacuum it is directly observable in e^+e^- annihilation, recall right panel of Fig. 1. Its structure suggests a decomposition into a nonperturbative low-mass regime, $M \leq 1$ GeV, saturated by hadronic resonances, a "dip" region for 1 GeV$< M \leq 1.5$ GeV, and a regime for $M > 1.5$ GeV where perturbation theory applies,

$$\mathrm{Im}\Pi_{\mathrm{EM}}^{\mathrm{vac}}(M) = \begin{cases} \displaystyle\sum_{v=\rho,\omega,\phi} \left(\frac{m_v^2}{g_v}\right)^2 \mathrm{Im}D_v^{\mathrm{vac}}(M)\,, & M < M_{\mathrm{dual}}^{\mathrm{vac}}\,, \\ \displaystyle -\frac{M^2}{12\pi}\left(1+\frac{\alpha_{\mathrm{s}}(M)}{\pi}+\ldots\right) N_c \sum_{q=u,d,s}(e_q)^2\,, & M > M_{\mathrm{dual}}^{\mathrm{vac}} \end{cases} \tag{6}$$

($N_c = 3$ is the number of colors and e_q the quark charge in units of the electron charge). Note that in the perturbative regime the final state in e^+e^- annihilation is still hadronic (with broad overlapping excited resonances such as ρ', ω', *etc.*), but the "long-distance" hadronization process does not affect the short-distance quark-production cross-section. This is often referred to as parton–hadron duality, which in the vector channel is realized for masses beyond a "duality threshold", $M > M_{\mathrm{dual}}^{\mathrm{vac}} \simeq 1.5$ GeV.

The inverse process of e^-e^+ annihilation is intimately related to the production rate of thermal dileptons from a heat bath of strongly interacting matter. It can be calculated starting from Fermi's Golden rule,

$$\begin{aligned} \frac{\Gamma_{ee}}{V} = \frac{dN_{ee}}{d^4x} \;=\; & e^4 \int \prod_i \frac{d^3p_i}{(2\pi)^3 2E_i} \prod_f \frac{d^3p_f}{(2\pi)^3 2E_f} 2\pi\delta(P_i - P_f - q) \\ & \times \langle i|j_\mu^{\mathrm{em}}|f\rangle\langle f|j_\nu^{\mathrm{em}}|i\rangle f^i\left(1 \pm f^f\right)\left(j_e^\mu \frac{1}{q^4} j_e^\nu\right), \end{aligned} \tag{7}$$

which can be cast into the form given in Eq. (1). This expression is leading order in the fine structure constant, $\mathcal{O}(\alpha_{\mathrm{EM}}^2)$, but exact in the strong interactions which are encoded in the spectral function (the leading order in the strong interaction is $\mathcal{O}(1)$). In the same framework one can calculate the thermal production rate of real photons as

$$q_0 \frac{dN_\gamma}{d^4x d^3q} = -\frac{\alpha_{\mathrm{EM}}}{\pi^2}\, f^B(q_0;T)\, \mathrm{Im}\Pi_{\mathrm{EM}}^T\,(M=0, q=q_0; \mu_B, T) \tag{8}$$

which only involves the transverse polarization of the EM spectral function. The leading orders of the photon rate are one lower in the EM coupling, $\mathcal{O}(\alpha_{\rm EM})$, but one higher in the strong coupling, $\mathcal{O}(\alpha_{\rm s})$, relative to the dilepton rate. This implies significant uncertainties in the magnitude of the rate even in the perturbative regime.

In the following three sections we focus on the dilepton rate in the soft (low-mass) regime, where the key issue is to determine the in-medium EM spectral function.

2.2. Hadronic matter

At low temperatures and densities, the appropriate degrees of freedom to describe strongly interacting matter are hadrons. In lukewarm matter, $T < m_\pi$, at vanishing baryon chemical potential, $\mu_B = 0$, the most abundant species are pions whose low-energy interactions are determined by the chiral Lagrangian. At higher temperatures, $T \geq m_\pi$, hadronic resonances quickly outnumber pions; much less is known about the chiral structure of resonance interactions (including excited nucleon states). However, it is still possible to write effective hadronic Lagrangians compatible with basic symmetry requirements and constrain their parameters by empirical information, *e.g.*, hadronic and radiative decay widths. The such constrained interactions can then be implemented into many-body theory to calculate in-medium selfenergies and spectral functions of hadrons. Clearly, the reliability of the predicted spectral functions largely hinges on the quality of the constraints applied to the effective interactions.

The above strategy has been adopted by several groups to compute the in-medium spectral function of the ρ meson (*cf.*, *e.g.*, the review papers [15, 16, 4, 17, 18] for a detailed discussion and further references). The special role of the ρ meson simply derives from its dominant contribution to the low-mass EM correlator where it outshines the ω by a factor of $\sim$ 10 (the constituent-quark model predicts a factor of 9, as inferred from Eq. (5); from the empirical dilepton decay widths one finds $\Gamma_{\rho\to ee}/\Gamma_{\omega\to ee} = (m_\rho^4/g_\rho^2)/(m_\omega^4/g_\omega^2) \simeq 11$). Starting point is a realistic description of the ρ properties in the vacuum. Usually the ρ is introduced into the chiral Lagrangian via a local gauge symmetry. To one loop order, the vacuum ρ selfenergy is built up from the standard $\rho \to \pi\pi$ diagram and a tadpole arising from the $\rho\rho\pi\pi$ 4-point vertex (the pertinent diagram has no imaginary part). With 3 free parameters (bare ρ mass, gauge coupling g and a regulator (cutoff) for the divergent loop integrals), a satisfactory reproduction of the ρ spectral shape as seen in the pion-EM formfactor and P-wave $\pi\pi$ scattering can be achieved, *cf.* Fig. 4 (the $\tau \to 2\pi\nu_\tau$ data are also well described, see Fig. 3). A good description of the entire spectral shape — not just its mass and width — is essential for later purposes of calculating low-mass dilepton spectra, especially below the free ρ mass.

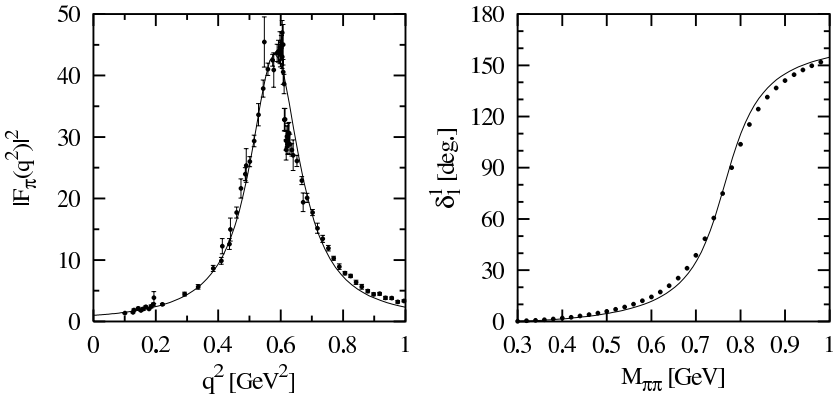


Fig. 4. Electromagnetic formfactor of the pion (left panel) and P-wave $\pi\pi$ scattering phase shifts (right panel) in the vacuum. An effective model assuming ρ-meson dominance with coupling to two-pion states is compared to data. Figures taken from Ref. [19].

Medium modifications of the ρ propagator,

$$D_\rho(M,q;\mu_B,T) = \frac{1}{M^2 - m_\rho^2 - \Sigma_{\rho\pi\pi} - \Sigma_{\rho M} - \Sigma_{\rho B}}\,, \tag{9}$$

are induced by (a) interactions of its pion cloud with hadrons from the heat bath, included in $\Sigma_{\rho\pi\pi}$ (*e.g.*, $\pi N \to \Delta$), and (b) direct ρ scattering off mesons (*e.g.*, $\rho\pi \to a_1$) and baryons (*e.g.*, $\rho N \to N^*$), denoted by $\Sigma_{\rho M}$ and $\Sigma_{\rho B}$, respectively. The medium effects in nuclear matter can be comprehensively constrained by analyzing $\pi N \to \rho N$ scattering and photoabsorption spectra on the nucleon and nuclei [20]. In this context, the pion cloud effects correspond to meson-exchange currents (*e.g.*, pion exchange in $\gamma N \to \gamma\Delta$), and the direct nucleon excitations, $\gamma N \to N^*, \Delta^*$, produce the resonance peaks in the cross-section. For the ρ interactions in a meson gas, one has to resort to the hadronic and radiative decay branchings of mesonic resonances with large coupling to ρ and γ final states, *e.g.*, $a_1 \to \pi\rho, \pi\gamma$ or $K_1 \to K\rho, K\gamma$ [21]. To date, for the case of cold nuclear matter, different calculations of the in-medium ρ spectral functions have reached agreement at a semi-quantitative level, and remaining discrepancies can be largely traced back to slight variations in the treatment of medium effects (*e.g.*, missing pion–cloud effects or linear-in-density approximations). An example for the ρ spectral functions under hot and dense conditions as expected for heavy-ion collisions at the CERN-SPS is displayed in the left panel of Fig. 5. The ρ resonance peak undergoes a strong broadening, indicative for its ultimate "melting" close to the phase transition. The medium modifications, especially the low-mass enhancement, are much reduced if baryon-induced effects are switched off, see right panel of Fig. 5.

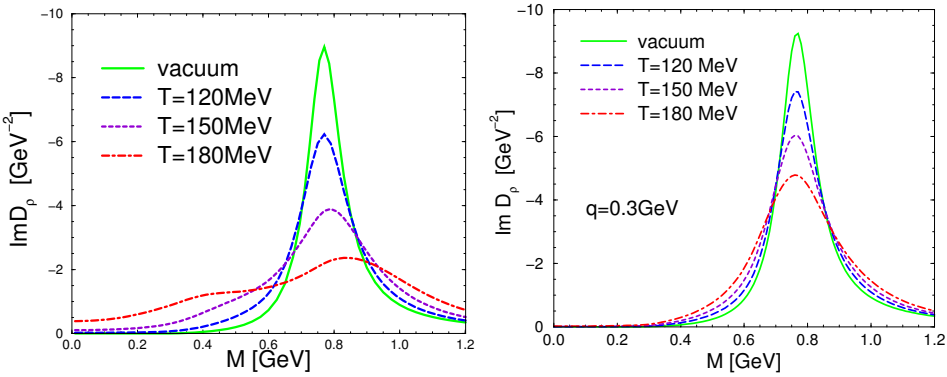


Fig. 5. Spectral function of the ρ meson in hot hadronic matter; left panel: in hot and dense matter for temperatures $T = 120$, 150 and 180 MeV and fixed baryon chemical potential of $\mu_B = 330$ MeV, corresponding to baryon densities of $0.1\varrho_0$, $0.7\varrho_0$ and $2.6\varrho_0$, respectively ($\varrho_0 = 0.16$ fm^{-3}); right panel: in a hot meson gas with all baryon-induced medium effects switched off.

Let us briefly allude to medium effects in the dip region, *i.e.*, for masses between 1 and 1.5 GeV. In this regime the continuum starts to develop, characterized by multi-meson contributions in the spectral function whose interactions with a medium are difficult to assess microscopically. Fortunately, one can make a more simple yet elegant argument based on chiral symmetry to estimate the medium effects on the spectral function. It was first developed in Ref. [22] for the finite-temperature case. Using current algebra in the chiral limit ($m_\pi = 0$), the interactions of the vector and axialvector correlators with a lukewarm pion gas were shown to result in their mutual mixing as

$$\Pi_{\rm V}(q) = (1-\varepsilon)\ \Pi_{\rm V}^{\rm vac}(q) + \varepsilon\ \Pi_{\rm A}^{\rm vac}(q) \tag{10}$$

(and likewise for the axialvector upon exchanging $V \leftrightarrow A$), with the mixing parameter $\varepsilon = T^2/6f_\pi^2$. The model-independent leading-temperature effect on the vector spectral function is an interaction with a thermal pion which reduces the strength at its resonance and moves it into the axialvector resonance. Such processes are of course included in the many-body treatment of the low-mass region discussed above, *e.g.*, via $\rho\pi \to a_1$ interactions. Here we use the mixing effect to predict that the dip region in the vector spectral function will be enhanced due to the admixture of the axialvector resonance (a_1). In fact, if one takes the τ decay data for the vacuum V and A spectral functions and carries the mixing all the way to the degeneracy point ($\varepsilon = 1/2$), one finds the intriguing result that the dip region is filled "precisely" to the level of the perturbative continuum, *cf.* Fig. 6. Stated

differently, chiral mixing induces the reduction of the in-medium duality threshold to $M_{\rm dual} \simeq 1$ GeV. The mixing effect is not enough to smear the ρ resonance — this is where the (higher-order) hadronic many-body effects come in, as we will see below. Similar arguments can be made for nuclear matter at zero temperature, where the role of the thermal pions is taken over by the virtual pion cloud of the nucleon [23, 24]; this is closely related to the pion cloud effects on the ρ meson through πN scattering discussed above.

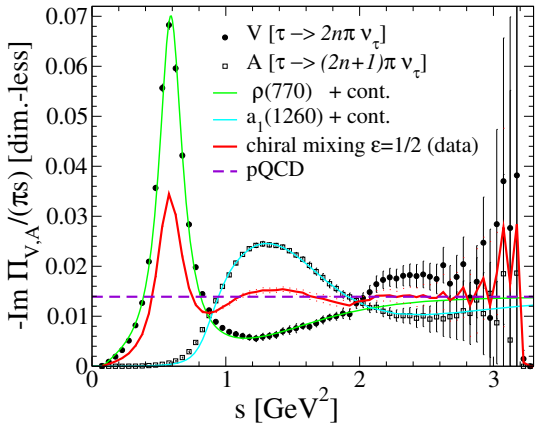


Fig. 6. Effect of chiral mixing [22] on isovector–vector (V) and –axialvector (A) spectral functions. When extrapolated to the chiral restoration point ($\varepsilon = 1/2$), the degenerate V and A spectral functions also degenerate with the perturbative continuum (dashed line) down to $s \simeq 1$ GeV^2, thus filling the "dip-region" in the vacuum V spectral function.

2.3. Quark-gluon plasma and lattice QCD

In a quark-gluon plasma (QGP) the leading source of thermal dileptons is the purely electromagnetic annihilation of two quarks of equal flavor, $q\bar{q} \to e^+e^-$, corresponding to a structureless noninteracting EM spectral function, $\mathrm{Im}\Pi_{\rm EM} \propto M^2$, as given by the lower line in Eq. (6). A consistent (gauge-invariant) calculation of loop corrections requires a careful treatment of infrared physics at the scale gT ($g = \sqrt{4\pi\alpha_{\rm s}}$) which can contribute at the same order as the leading term (due to soft propagators of the type $1/(t - m_D^2)$ with $m_D \sim gT$, canceling the extra coupling constants in the vertices). A systematic way to resolve these problems is provided by resummations within hard-thermal-loop (HTL) perturbation theory, which has been first applied to thermal dilepton production in Ref. [25]. The softening of the in-medium quark dispersion relation, developing plasmino branches as well as Landau damping, in the quark–antiquark loop produce

an appreciable enhancement of the HTL dilepton rate (or EM spectral function) over the free one, not unlike the medium effects in the pion cloud of the ρ. The enhancement is present for a rather wide regime around $q_0 \sim gT$, and growing with decreasing q_0.

In more recent years, the problem of soft dilepton emission has been addressed from first principles using lattice QCD (lQCD) [26,27], by computing the thermal expectation value of current–current correlation in Eq. (3) for Euclidean time, τ, and Fourier-transforming it as

$$\Pi_{\mu\nu}\,(\tau,\vec{q}) = \int d^3x\ \Pi_{\mu\nu}\,(\tau,\vec{x})\,e^{i\vec{p}\cdot\vec{x}}\,. \tag{11}$$

In a heat bath in equilibrium, the imaginary-time coordinate, τ, is not related to dynamical but statistical properties of the system: the temperature comes in through a periodicity in τ, effectively limiting the latter to the "Matsubara circle", $0 \le \tau \le 1/T$. The connection to the time-like (observable) spectral function can be established by means of a Kramers–Kronig dispersion relation leading to

$$\Pi(\tau,q;T) = \int_0^\infty \frac{dq_0}{2\pi}\ \rho(q_0,q;T)\ \frac{\cosh[q_0(\tau-1/2T)]}{\sinh[q_0/2T]}\,, \tag{12}$$

where $\rho(q_0,q;T) = -2\ \mathrm{Im}\Pi_i^i$ is the polarization-summed spectral function (in the vector channel, charge conservation implies the 00-component to proportional to $\delta(q_0)$). Equation (12) illustrates a notorious problem of extracting spectral functions from Euclidean correlators computed in lQCD: one needs to perform an inverse integral transform on a finite number of meshpoints in τ, which additionally carry statistical and systematic uncertainty and are limited to the Matsubara circle. Nevertheless, probabilistic methods (known as maximum entropy method, successfully used, *e.g.*, in image reconstruction) can be applied which are usually coupled with additional physical constraints such as positivity of the spectral function [28]. However, it currently remains unclear as to how much structure can be resolved in the spectral functions (*e.g.*, resonance peaks *vs.* threshold enhancements). In Ref. [27], this problem has been mitigated by making a physically motivated ansatz for the EM spectral function and fitting its 3 free parameters to the euclidean correlator "data". The ansatz consists of a Breit–Wigner "transport" peak at low energies plus a pertubative continuum with α_s correction (plus Pauli-blocking factor) at high energies, as in the lower line of Eq. (6). The resulting spectral function in a gluon plasma of temperature $1.45\,T_c$ (without thermal anti-/quarks) is shown as the solid black line in left panel of Fig. 7. It is divided by the energy variable to exhibit

the "transport peak" for $q_0 \to 0$ which is dictated by the proper low-energy limit of the retarded correlator, $\rho^{ii}_{\rm EM}(q_0 \to 0; T) \propto \sigma_{\rm EM}(T)\, q_0$, where $\sigma_{\rm EM}$ denotes the electrical conductivity (a transport coefficient of the strongly interacting medium). Also shown are the vacuum correlator and the results of the hadronic many-body calculations predicting a strongly broadened ρ meson at a temperature close to $T_{\rm c}$. Despite the seemingly quite different environments (gluon plasma *vs.* interacting hadron gas) the two in-medium calculations are very different from the vacuum shape, but *not* very different from each other. In fact, a cleaner comparison can be done by going back to the Euclidean correlators, by simply performing the integral over the hadronic many-body spectral function in Eq. (12). The resulting correlators (normalized to the noninteracting one) for the vacuum and in-medium spectral function are compared to the direct lQCD computations in a gluon plasma in the right panel of Fig. 7. The in-medium spectral function leads to a correlator ratio quite similar to the one from lQCD, while the lack of a low-mass enhancement in the vacuum spectral function entails a ca. 50% underestimate of the maximum in $\Pi(\tau = 1/2T)$ (the Euclidean correlators are symmetric about the midpoint of the Matsubara circle, $\tau = 1/2T$). The rather good agreement of the in-medium correlators suggests that the latter

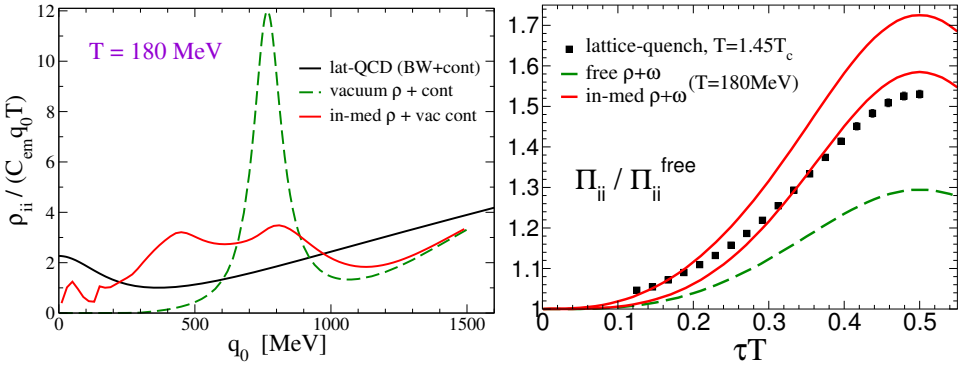


Fig. 7. Left panel: EM spectral functions, at vanishing 3-momentum and summed over polarization, from thermal lQCD at $T = 1.45\ T_{\rm c}$ (solid black line) [27], as well as for vacuum and in-medium hadronic calculations at $T = 180$ MeV (dashed and red solid line, respectively) [29]. The spectral functions are rendered dimensionless upon division by energy and temperature, and normalized by charge isospin degeneracy ($C_{\rm em} = \sum_{u,d} e_q^2 = 5/9$ for lQCD and $C_{\rm em} = 1/2$ for the isovector hadronic results). Right panel: euclidean correlators corresponding to the spectral functions in the left panel (squares: lQCD; solid lines: in-medium hadronic with the free continuum (lower line) and one with a threshold lowered by 0.3 GeV (upper line); dashed line: vacuum; the hadronic calculations additionally include the contribution from free or in-medium ω spectral functions).

are not particularly sensitive to detailed structures in the spectral function, but that they contain valuable information on a redistribution of strength to low energies and on the transport peak.

2.4. In-medium diletpon and photon rates

It is now straightforward to convert the EM spectral functions discussed in the previous two sections into thermal emission rates of dileptons, *cf.* Fig. 8. The left panel confirms that the strong broadening of the ρ spectral function, together with the chiral mixing in the dip region, make the hadronic rate approach the partonic-based calculations, in particular the HTL-improved result. In Ref. [29] this has been interpreted as an in-medium reduction of the quark–hadron duality threshold in hadronic matter with increasing temperature and density: the hadronic rate successively approaches the perturbative partonic rate, with $M_{\rm dual} \to 0$ in the vicinity of $T_{\rm c}$ (or somewhat above). On the one hand, this implies an approach to chiral restoration, since the perturbative rate is chirally restored, *i.e.*, degenerate with the axialvector. On the other hand, it also implies an approach to deconfinement, as signaled by the transition to a more economic (perturbative) description in terms of partonic degrees of freedom. This picture is now further corroborated by the most recent lQCD results [27]; the right panel of Fig. 8 exhibits a rather close agreement of the nonperturbative lQCD rate with the HTL rate (except at very small energies $q_0 \ll gT$ where the latter receives additional corrections).

In Ref. [30], a "more realistic way" to interpret quark–hadron duality has been suggested, by advocating the 3-volume multiplied production rates, $V dR/dM^2$, as the relevant quantities to compare. This is to account for the potentially rather different 3-volumes of hadronic and QGP phases if considering a system at fixed entropy (which is a good approximation for a fireball in URHICs). However, the thermal production rates are thermodynamically intensive quantities, well-defined in the infinite-volume limit (in which case one should not multiply with a volume factor). Furthermore, as discussed in the introduction, the finite-T QCD phase transition is most likely not a sharp one, especially concerning deconfinement. Recall that the increase in the degrees of freedom observed in the thermodynamic state variables such as energy density is well accounted for by the increasing population of states in the hadronic resonances gas [6]. It is precisely this increase (a precursor of the so-called the "Hagedorn" catastrophe) which leads to a likewise increase in the ρ width thus signaling its melting. In other words, the increase in degrees of freedom, which is ultimately responsible for a reduced volume at fixed total entropy in a finite system, is a hadronic effect, which, in turn, is at the origin of the ρ melting (as can be seen by glancing at the right panel of Fig. 13 below).

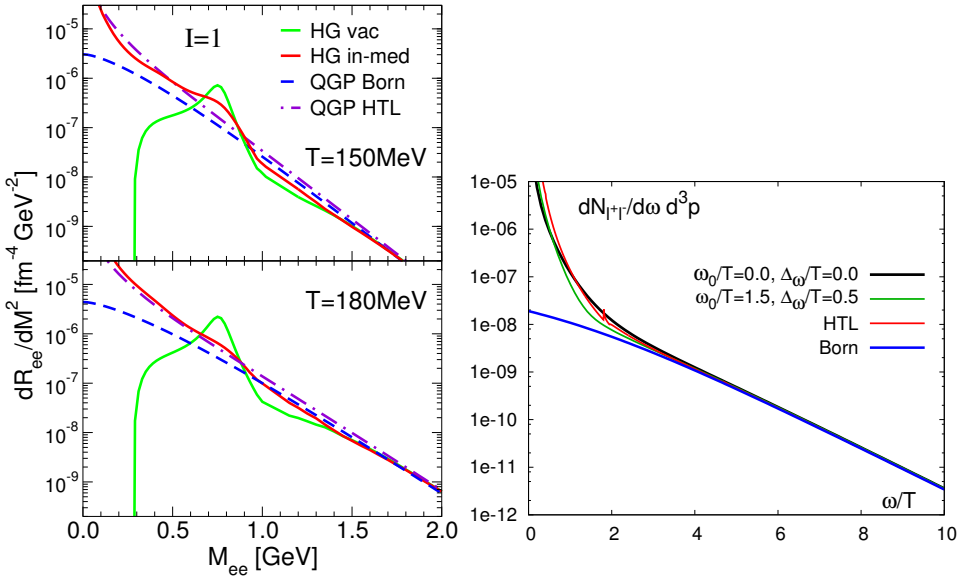


Fig. 8. Thermal dilepton rates; left panel: from a hadron gas with vacuum (solid gray/green line) and in-medium [29] (solid black/red line) EM spectral function, compared to $q\bar{q}$ annihilation in leading-order (dashed line) and with hard-thermal loop corrections [25] (dashed-dotted line); all rates are integrated over the pair 3-momentum; right panel: from quenched lattice QCD at 1.45 T_c [27] as extracted from the Euclidean correlator shown in Fig. 7 (black and gray/green lines), also compared to LO and HTL calculations, all at vanishing pair 3-momentum. Right figure taken from Ref. [27].

Thermal photon rates from the hadronic and QGP phase are compiled in Fig. 9. As elaborated following Eq. (8), photon production processes from a medium of on-shell particles require a scattering process and are therefore nontrivial to leading order in the strong coupling (*e.g.*, $\pi\rho \to \pi\gamma$ or $qg \to q\gamma$). However, in consistently resummed many-body calculations of the EM spectral function, the latter possesses a nonzero $M \to 0$ limit at finite 3-momentum, see, *e.g.*, the ρ spectral function in the left panel of Fig. 5 (if additionally $q \to 0$ one obtains the electric conductivity). This has been used in Ref. [31] to extract the photon production rates encoded in the hadronic spectral function of Ref. [29], corresponding to processes of type $\pi\rho \to a_1 \to \gamma$, $N\rho \to N^* \to N\gamma$ or pion t-channel exchange in $\pi N \to \gamma N$ included in $\Sigma_{\rho M}$, $\Sigma_{\rho B}$ and $\Sigma_{\rho\pi\pi}$, respectively (*cf.* the solid blue line in Fig. 9). Additional t-channel meson-exchange reactions become important at photon momenta $q > 1$ GeV (*cf.* the dashed line in Fig. 9), most notably ω exchange in $\pi\rho \to \pi\gamma$. These rates are compared to QGP-based calculations,

specifically to the LO HTL rate derived in Ref. [32],

$$q_0 \frac{dR_\gamma}{d^3q} = \frac{6}{9}\frac{\alpha\alpha_S}{2\pi^2} T^2 e^{-q_0/T} \ln\left(1 + \frac{2.912}{4\pi\alpha_s}\frac{q_0}{T}\right) , \tag{13}$$

for $N_f = 3$ light flavors and with an added "1" in the logarithm to regularize its infrared behavior (surprisingly, the such obtained electric conductivity is not far from the one computed in thermal lQCD discussed in Sec. 2.3). This expression nicely illustrates the leading $\mathcal{O}(\alpha_s\alpha)$ behavior of the photon rate. It turns out, however, that there are additional contributions at this order, requiring a full resummation of ladder diagrams. This has been achieved in Ref. [33]. The numerical result of this work exceeds the "naive" LO rate by about a factor of 2–3, *cf.* Fig. 9. When comparing QGP and total hadronic rates (the sum of the two contributions plotted in Fig. 9), one again finds that both are very comparable at a temperature of $T = 200$ MeV (chosen mostly for historic reasons). Thus photon rates also support the duality hypothesis, although the theoretical control over the calculations is less good as in the dilepton case.

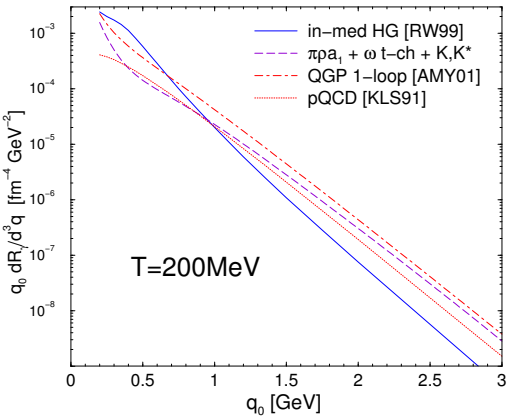


Fig. 9. Thermal photon rates from hadronic matter [31] (solid (blue) line: vector spectral function [29] at the photon point; dashed line: t-channel meson-exchange reactions) and from the QGP (dotted (red) line: LO HTL calculation [32], dashed-dotted line: complete resummed LO result [33]).

3. Dilepton and photon spectra in heavy-ion collisions

To date, dilepton spectra in heavy-ion collisions have been measured at the SPS($\sqrt{s} = 17.3$, 8.7 AGeV) [34, 35, 36, 37, 38, 39], at RHIC ($\sqrt{s} =$ 200 AGeV) [40, 41] and at lower energies at BEVALAC and SIS ($E_{\rm lab} = 1$–2 AGeV) [42, 43], see, *e.g.*, Refs. [44, 45] for recent experimental reviews. In

this section we apply the rates discussed above to calculate thermal-emission spectra from URHICs, focusing our comparison on recent highlights from data at SPS and RHIC. Two additional ingredients are required to do so: a realistic space-time evolution of the expanding fireball formed in the reaction and an assessment of nonthermal sources contributing to the thermal spectra (in some cases it is possible to subtract these experimentally).

Basic elements of a realistic fireball are summarized in Sec. 3.1, while nonthermal sources are addressed on a case-by-case basis of each observable. The analysis of experimental spectra is organized according to their putative information content, namely in-medium effects on spectral properties in connection with the emission duration (Sec. 3.2) and temperature and expansion characteristics of the source (Sec. 3.3).

3.1. Space-time evolution of heavy-ion collisions

Much has been learned about the space-time evolution of the medium formed in URHICs from the wealth of available hadron abundances, $p_{\rm t}$ spectra and elliptic flow. Generally, hydrodynamic models do well in describing the latter two (especially at RHIC and LHC) up to momenta of $p_{\rm t} =$ 2–3 GeV [3]. This encompasses more than 90% of the observed particles, and justifies the notion of a collectively expanding medium in local thermal equilibrium where the pressure gradients drive the acceleration. This mechanism works well enough to have predicted azimuthal asymmetries in the $p_{\rm t}$ spectra for noncentral heavy-ion collisions: the elliptic asymmetry given by the transverse overlap zone of the colliding nuclei leads to larger pressure gradients along the short axis of the ellipsoid, which in turn provide larger acceleration resulting in a positive "elliptic flow" coefficient, $v_2(p_{\rm t})$, in the angular distribution of the hadron $p_{\rm t}$ spectra (this is arguably the strongest evidence for the celebrated "near-perfect liquid" discovered at RHIC). Taking all evidence together, the following picture emerges: Shortly after the collision of the two nuclei, at a thermalization time of $\tau_0 = 0.5$–1 fm/c, most of the entropy has been produced and the system has thermalized into a QGP, with initial temperature of *ca.* $T_0 = 350$–400 MeV (200–250 MeV at SPS, $\sim$ 500–600 MeV at LHC). The QGP expands for about 3 fm/c before entering the transition regime to hadronic matter at around $T_{\rm c} \simeq 170$ MeV, where it spends almost 5 fm/c. At this point the hadronic abundances become frozen, leading to the notion of "chemical freezeout" where the inelastic reactions are believed to turn off. In the subsequent hadronic phase, elastic scattering driven by hadronic resonances is still operative leading to a further cooling of the system for about 5–10 fm/c until "thermal freezeout" occurs at $T_{\rm fo} \simeq 100$ MeV. After this, hadrons stream freely to the detector (modulo long-lived electromagnetic and weak decays). Figure 10 summa-

rizes typical trajectories in the QCD phase diagram, as well as the time dependence of temperature, for central heavy-ion collisions at SPS, RHIC and LHC. Besides initial conditions and the equation of state, hydrodynamic models require the implementation of "freezeout". At thermal freezeout, the medium is converted into hadron spectra using the time-honored Cooper–Fry prescription. "Chemical freezeout" implies that in the subsequent evolution the abundances of observed (stable) hadrons should be conserved. This is achieved by introducing effective chemical potentials into the hadronic equation of state (usually modeled via a hadron resonance gas), to individually conserve the number of pions, kaons, nucleons and antinucleons (not only their difference, which is an exact conservation law related to the baryon chemical potential, μ_B), *etc.* [46]. For dilepton (photon) production this implies that, *e.g.*, the process $\pi\pi \to \rho \to e^+e^-$ ($\pi\rho \to \pi\gamma$) is augmented by a pion fugacity squared, z_π^2 (z_π^3), where $z_\pi = \exp(\mu_\pi/T)$.

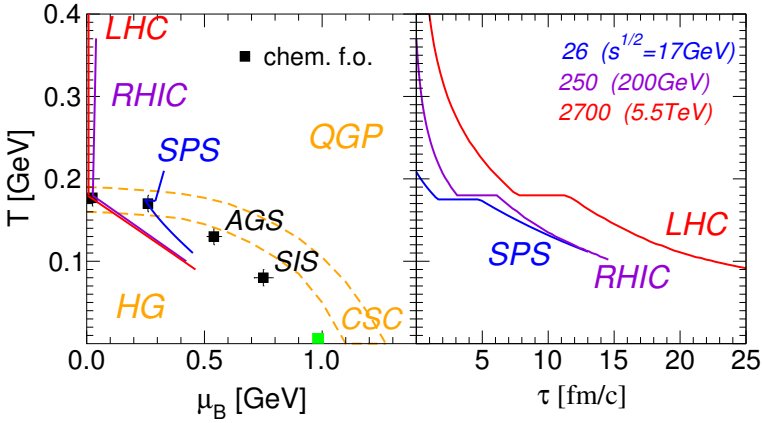


Fig. 10. Schematic representation of isentropic trajectories that the medium follows in URHICs at SPS, RHIC and LHC in the QCD phase diagram (left panel) and when projected on the temperature axis as a function of time using hadron spectra to estimate the collective expansion properties (right panel). Each trajectory is calculated for a fixed specific entropy, $S/N_B = s/\varrho_B$, according to entropy and baryon-number conservation. In addition, the hadronic part of the trajectories implements effective chemical potentials for all strongly stable hadrons [46] to maintain the observed hadron ratios as determined by thermal-model fits at chemical freezeout [1] characterized by the "data points".

Before going into quantitative theory comparisons to data, it is instructive to make a more general assessment of which stages of the fireball evolution will contribute at which dilepton energies/masses in the spectra. Toward this goal we write the time-differential invariant-mass spectrum, integrated over 3-momentum and 3-volume at each time snapshot, as [10]

$$\begin{aligned}\frac{dN_{ee}}{dMd\tau} &= \frac{M}{q_0}\int d^3x\; d^3q\; \frac{dN_{ee}}{d^4xd^4q} \\ &\simeq \text{const.}\; V_{\rm FB}(\tau)\; \frac{{\rm Im}\Pi_{em}(M;T)}{M}\int \frac{d^3q}{q_0}\; {\rm e}^{-q_0/T} \\ &\simeq \text{const.}\; V_{\rm FB}(\tau)\; \frac{{\rm Im}\Pi_{em}(M;T)}{M^2}\; {\rm e}^{-M/T}\; (MT)^{3/2}\,, \end{aligned} \tag{14}$$

where $V_{\rm FB}$ denotes the volume of the expanding fireball. For the second (approximate) equality it has been assumed that the in-medium EM spectral function depends only weakly on 3-momentum (which is exact in vacuum due to Lorentz-invariance, and approximately satisfied in medium for not too large momenta). For the third (approximate) equality we have invoked the nonrelativistic approximation, $T/M \ll 1$. In a last step, we relate the fireball-evolution time to the temperature, $T(\tau)$, to obtain the temperature-differential emission as

$$\frac{dN_{ee}}{dMdT} \propto {\rm Im}\,\Pi_{\rm EM}(M;T)\; {\rm e}^{-M/T}\; T^{-m}\,. \tag{15}$$

The power of temperature, m, depends on the details of the fireball expansion (*e.g.*, 1-D Bjorken or full 3-D as appropriate for the early and late phases, respectively), and the equation of state (*i.e.*, the power law of entropy density, $s \propto T^n$, with $n = 3$ for an ideal massless gas, but larger for a hadron-resonance gas), see Ref. [10] for more details. In Fig. 11 we plot the coefficient $f(T;M) = \exp(-M/T)\; T^{-m}$ as a function of temperature for different masses. At each mass, the maximal emission yields are centered around a temperature $T_{\rm max} \simeq T/m \simeq T/5$ which reflects the competition between the thermal exponential, favoring high temperature, and the increasing 3-volume of the fireball as it expands and cools. Note that for low-mass dilepton emission, $M \leq 1$ GeV, the profile function, $f(T;M)$, peaks in the hadronic phase of the evolution. On the one hand, medium effects in the EM spectral function, which lead to a marked enhancement for $M < m_\rho$ with increasing T and ϱ_B (recall Fig. 5), will shift this peak to somewhat larger T (note, however, that the low-mass enhancement tends to saturate when approaching $T_{\rm c}$, see Fig. 8 left). On the other hand, the latent heat burned off in the hadron-to-parton transition, *i.e.*, the rapid rise of s/T^3 in the vicinity of the phase conversion, will bias the emission to the hadronic phase. Both effects lead to an additional focusing of low-mass dilepton emission to hot and dense hadronic matter.

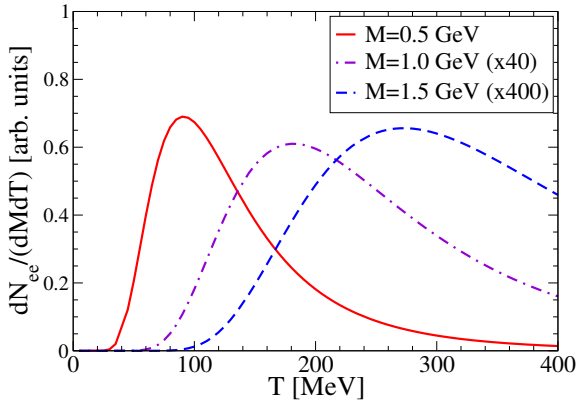


Fig. 11. Emission yields of thermal dileptons as a function of temperature for different values of their invariant mass, assuming a temperature independent EM spectral function.

Similar arguments apply to thermal photon (or dilepton) transverse-momentum spectra, with an important amendment due to the transverse flow of the fireball causing a spectral blue shift (well-known from hadron spectra). Since the flow develops over time, it creates a bias toward the later emission stages.

3.2. Spectrometer and chronometer

The state-of-the art in dilepton measurements in URHICs has been set by the NA60 Collaboration with their dimuon data from In–In ($\sqrt{s}$ = 17.3 AGeV) collisions at the SPS [36,38]. Excellent statistics combined with superb mass resolution allowed for a subtraction of background sources thus isolating the "excess radiation" from reinteractions in the fireball. In addition, a full acceptance correction could be carried out so that the invariant-mass spectra, displayed in the left panels of Fig. 12, are, for the first time, truly *invariant*. This, in particular, implies that blue-shift effects of the expanding fireball do not distort the spectra. The result is quite stunning: the data show a near-perfect thermal spectrum, "only" modulated by a broad bump around the free ρ/ω masses. Even without any fireball convolution, a comparison to the theoretical input rates calculated in Ref. [15] (shown in the left panel of Fig. 8, supplemented with dimuon threshold kinematics) exhibits a remarkable agreement for an average temperature of 150–160 MeV. This temperature is tantalizingly close to the most recent lQCD predictions shown in the left panel of Fig. 2, provoking the conclusion that the chiral transition has been observed at SPS! Of course, these rather general arguments need to be backed up by quantitative calculations convoluting the T- and ϱ_B-dependent emission rates over a realistic fireball expansion (as

discussed in Sec. 3.1). This has been done in Ref. [47] and the results are in very good agreement with the data as seen in the upper left panel of Fig. 12. Subleading contributions include the decays of ω and ϕ mesons, a nonthermal component of ρ mesons, and Drell–Yan annihilation. Especially the latter two play a significant role when high-q_{t} cuts are imposed on the spectra (this is fully in line with the standard notion from hadron p_{t} spectra that the thermal component dominates up to $p_{\mathrm{t}} \simeq 2\,\mathrm{GeV}$ yielding to "hard production" above). With the level of precision set by the NA60 mass spectra several further diagnostics of the produced medium become available, as discussed in the following.

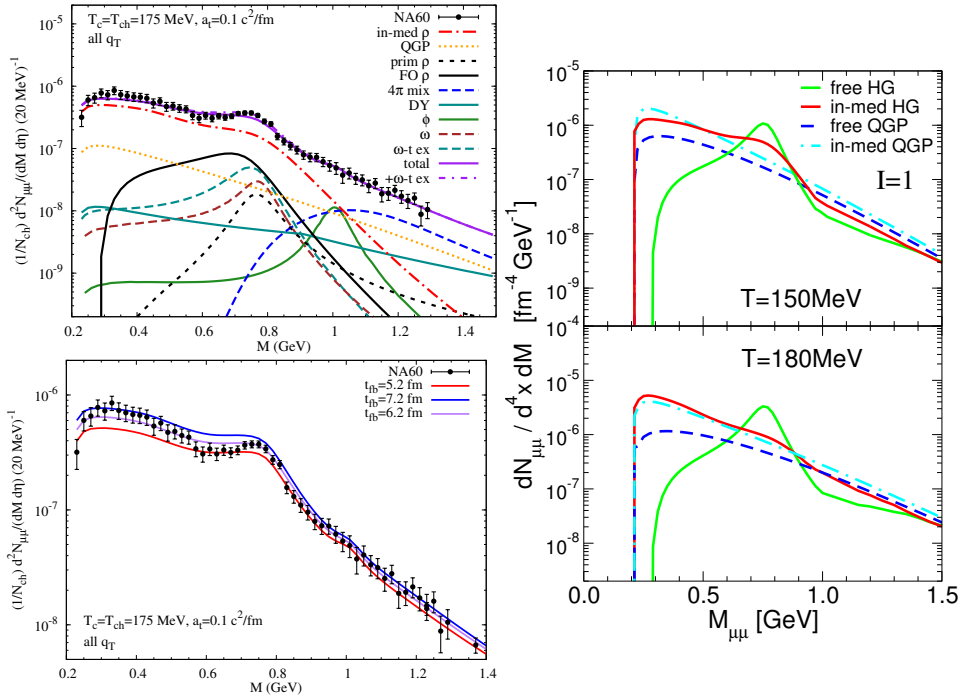


Fig. 12. Left panels: excess dimuon invariant-mass spectra as measured in In–In ($\sqrt{s} = 17.3\,\mathrm{AGeV}$) collisions at the SPS [38, 39], compared to theory calculations with in-medium hadronic spectral functions and QGP emission from an expanding fireball [47]. The upper panel resolves the individual contributions in the calculation which, however, are dominated by the in-medium ρ spectral function at low-mass and a combination of hadronic continuum ("4π") and QGP radiation at intermediate mass. The in-medium ρ plus 4π make up the total in-medium hadron-gas (HG) rate shown by the solid (red) line in the right panels for two temperatures (including baryon-density effects) [15]. The lower left panel illustrates the effect of varying the fireball lifetime in the calculation.

The first obvious question is how sensitive the mass spectra are to the ρ-meson spectral shape. This has been tested qualitatively by switching off the medium effects induced by baryons, *i.e.*, using the T-dependent ρ spectral function in a hot meson gas as displayed in the right panel of Fig. 5. The resulting $\mu^+\mu^-$ spectra are in stark disagreement with the NA60 data, *cf.* left panel of Fig. 13: the low-mass enhancement is underestimated by about a factor of ~ 4, and the yield in the ρ-peak region is overestimated by about a factor of ~ 2, both several standard deviations away from experiment. The evolution of the ρ width (taken as full-width-half-maximum in the spectral function) along the SPS trajectory used in the calculations is displayed in the right panel of Fig. 13. The upper curve (circles), corresponding to the full calculation, confirms that the "average width" of $\bar{\Gamma}_\rho^{\rm med} \simeq 350$–$400\,$MeV reflects the conditions of the medium close to the chiral transition. It also exhibits a rather strong rise for temperatures beyond that. This rise becomes even more pronounced in chemically equilibrated matter where the effective meson-chemical potentials are switched off (squares; at fixed s/ϱ_B this also implies a slight reduction in μ_B). It is not unlike the increase of the thermodynamic state variables in the hadron-resonance gas around a similar temperature. No such behavior emerges at comparable temperatures if baryon-induced medium effects are switched off. Since the average width implies the occurrence of larger widths in the course of the medium expansion, a situation with $\Gamma_\rho^{\rm med} \simeq m_\rho$ must be realized, *i.e.*, resonance melting.

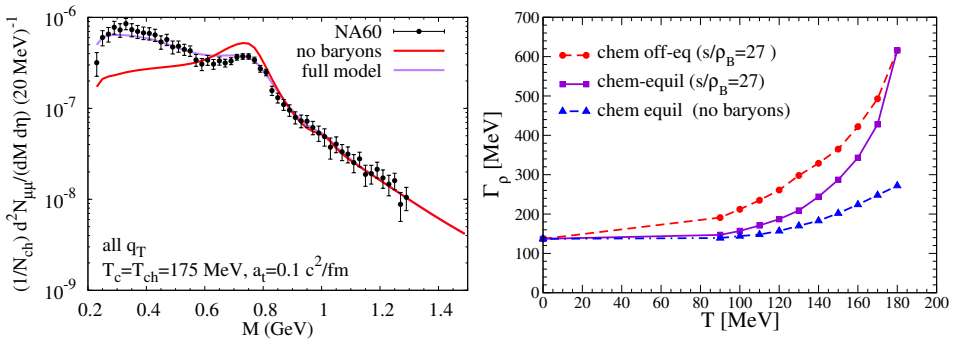


Fig. 13. Left panel: comparison of the acceptance-corrected NA60 mass spectra in In–In ($\sqrt{s} = 17.3\,$AGeV) collisions [38,39] to a calculation where baryon-induced effects ion the EM spectral function have been switched off. Right panel: in-medium ρ widths (estimated from the full-width-half-maximum of its spectral function) along the SPS trajectory used in the spectra calculations projected on the temperature axis, for the full calculation including effective chemical potentials (circles) and in chemical equilibrium with (squares) and without (triangles) baryon-induced effects; figure taken from Ref. [4].

It is important to note that baryon-induced medium effects remain a key player at RHIC [48]. This is so because the ρ equally interacts with baryons (B) and anti-baryons ($\bar{B}$) due to CP invariance of strong interactions (the ρ is a CP eigenstate). Therefore, the sum (not the difference) of ϱ_B and $\varrho_{\bar{B}}$ is the relevant quantity for medium effects. At RHIC, the rapidity density of baryons plus antibaryons is slightly larger than at SPS, while the pion rapidity density is roughly a factor of 2 larger, implying an accordingly increased fireball volume at given temperature. Thus, the "effective" density $\varrho_{\rm eff} \equiv \varrho_B + \varrho_{\bar{B}}$, is not very different at SPS and RHIC, and probably also at LHC. From a theoretical point of view, the configuration of small net-baryon chemical potential at collider energies is appealing because it comes closest to $\mu_B = 0$ where lQCD computations are most powerful.

While the spectral shape of the NA60 data could be predicted by theory, the total yields could not, at least not within the experimental accuracy. However, one can turn the argument around and utilize the total yield as a precision clock for the emission duration. In previous analyses of dilepton spectra in Pb–Au collisions by CERES [34], the fireball lifetime estimated from hydrodynamic models, $\tau_{\rm FB} \simeq 10$–$15\,{\rm fm}/c$, resulted in a reasonable description of the e^+e^- excess radiation [29]. The precision attained with the NA60 data is significantly increased: even a variation of $\pm 1\,{\rm fm}/c$ in the calculation discussed above leads to noticeable deviations from the data, *cf.* lower left panel of Fig. 12. The resulting "measurement" of $\tau_{\rm FB} = 6.5 \pm 1\,{\rm fm}/c$ for the fireball lifetime using dilepton yields is probably the most accurate one thus far in URHICs (it is not to be confused with the pion emission duration referred to in Hanbury–Brown Twiss (HBT) interferometry measurements).

Let us briefly comment on the current situation of low-mass dilepton measurements at RHIC. The PHENIX Collaboration found a very large enhancement for masses below the free ρ mass in central Au–Au ($\sqrt{s} = 200\,{\rm AGeV}$) collisions [40] which is largely concentrated at low transverse momenta, $q_{\rm t} < 0.5\,{\rm GeV}$. It cannot be explained by the theoretical ingredients which allow for an understanding of the SPS dileptons. The STAR collaboration, on the other hand, reports a smaller enhancement [41], which, however, is still sizable and roughly consistent with theoretical expectations.

3.3. Thermometer and barometer

Historically, the best experimental tool to serve as a "thermometer" of the early phases in URHICs was believed to be thermal radiation of photons. With a structureless emission rate, the slope of the spectrum is directly related to the temperature of the system, modulo a blue-shift from transverse expansion which is expected to be small in the early stages. At SPS energies, the presence of a significant excess signal of photons, *i.e.*, beyond

those from initial production and final-state decays of long-lived hadrons (mostly $\pi^0, \eta \to \gamma\gamma$), remains inconclusive [49]. At RHIC, however, the PHENIX collaboration has observed a strong excess signal in semi-/central Au–Au collisions [50] for transverse momenta above $q_t = 1\,\mathrm{GeV}$ up to at least 3–4 GeV, beyond which the primordial production extrapolated from binary N–N collisions dominates, see left panel of Fig. 14 ("excess" plus "primordial" are usually referred to as "direct" photons, *i.e.* long-lived decays subtracted). This range nicely coincides with theoretical expectations of where the QGP radiation is most visible [16,31,51,52,53,54]. The inverse slope of the excess radiation was found to be consistent with an exponential with temperature $T = 221 \pm 19^{\mathrm{stat}} \pm 19^{\mathrm{sys}}\,\mathrm{MeV}$. This seems to point at a source well inside the QGP, albeit not to the very early phases where temperatures above 300 MeV are expected, recall Fig. 10.

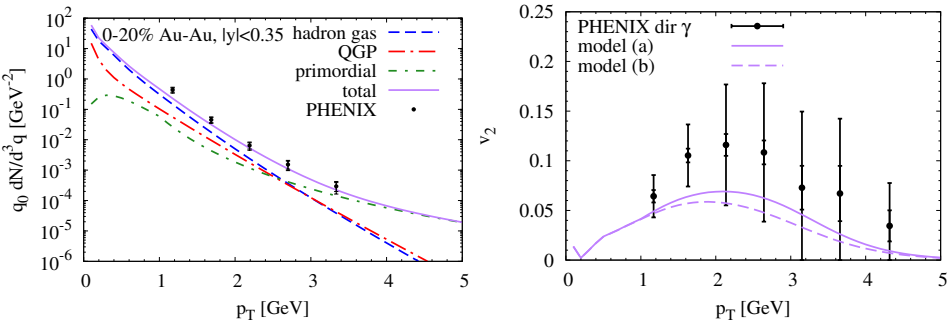


Fig. 14. Transverse-momentum spectra (left panel) and elliptic flow (right panel) of direct photons in 0–20% central Au–Au ($\sqrt{s} = 200\,\mathrm{AGeV}$) collisions at RHIC, compared to PHENIX data [50,55]. The curves are calculations [56] with a realistic fireball evolution employing thermal QGP and hadronic rates which are "dual" around T_c, corresponding to Fig. 9.

Maybe even more intriguing are the recent PHENIX measurements of the direct-photon elliptic flow [55], *cf.* right panel of Fig. 14. In the regime of the excess radiation, *i.e.*, for $q_t \leq 3\,\mathrm{GeV}$, the elliptic-flow coefficient, $v_2(q_t)$, is comparable to those of pions, which are only emitted at the end of the fireball evolution, *i.e.*, with maximal v_2. On the contrary, the excess photons are supposed to be emitted throughout the evolution (including early, where the v_2 is still small), and the primordial ones should carry zero v_2. More quantitatively, predictions of thermal-photon v_2 using hydrodynamic models with QGP-dominated excess radiation lead to maximal values of $v_2 \simeq 2\%$ for direct photons in 0–20% Au–Au ($\sqrt{s} = 200\,\mathrm{AGeV}$) collisions [51, 52, 53, 54], well below the PHENIX data. In these calculations the hadronic emission rates were significantly smaller than the QGP rate in the vicinity of T_c, which differs from the "duality" hypothesis suggested by Fig. 9. In

Ref. [56] we therefore revisited our earlier calculations of direct photons [31] by refining the thermal fireball model as to quantitatively describe the p_t spectra and elliptic flow of bulk hadrons, freezing out at $T_{fo} \simeq 100\,\text{MeV}$, and multistrange hadrons, kinetically decoupling close to chemical freezeout, $T_{ch} \simeq 180\,\text{MeV}$. This, in particular, led to harder thermal photon spectra from the hadronic phase, thus exceeding the QGP contribution over the for thermal emission relevant q_t range up to 3–4 GeV. Consequently, the thermal-photon v_2 increases substantially, now being dominated by hadronic emission where most of the final v_2 has already been built up. The resulting direct-photon $v_2(q_t)$, which includes the primordial component (extrapolated from pp collisions) with vanishing v_2, reaches up to 6–7%, a factor of ~ 3 larger than in previous calculations and thus much closer to experiment, *cf.* right panel in Fig. 14.

With dominantly hadronic emission, one should revisit the evaluation of the photon slope parameter. For this purpose, we plot in the left panel of Fig. 15 the blue-shifted effective temperature as a function of time in the underlying fireball evolution,

$$T_{\text{eff}} \simeq T\sqrt{\frac{1+\langle\beta\rangle}{1-\langle\beta\rangle}}\,, \tag{16}$$

where T is the "true" temperature in the thermal rest frame and $\langle\beta\rangle$ the average transverse flow velocity (typically 2/3 of the surface velocity). The comparison to the PHENIX measurement reveals that the largest overlap is indeed inside the hadronic phase, for a broad temperature interval around $\sim$130 MeV, "Doppler-shifted" by about 100 MeV. This is consistent with the large elliptic flow.

Similar analysis can be carried out for dileptons, which has been done with the NA60 dimuon q_t-spectra at the SPS [38]. The extracted slope parameters are displayed as a function of the invariant-mass window imposed on the q_t spectra in the right panel of Fig. 15. One finds a continuous rise of T_{eff} with mass, roughly following the schematic (nonrelativistic) analogue of Eq. (16) for massive particles (here: virtual photons),

$$T_{\text{eff}} \simeq T + M\langle\beta\rangle^2\,. \tag{17}$$

This corroborates the hadronic nature of low-mass dileptons below the ρ mass. However, above the ρ mass, the slopes decrease, which has been argued to signal a transition to a new source with small flow and thus of partonic nature. However, the latter part of the interpretation is not unique and one should keep in mind the following features: (a) the ρ-mass region, $M \simeq 0.7$–$0.9\,\text{GeV}$, is predominantly populated by contributions from the late fireball stages, since the ρ spectral shape is recovering its vacuum form which

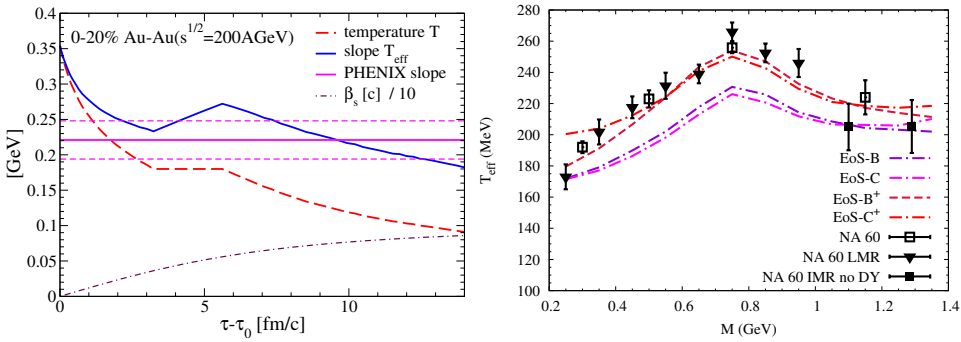


Fig. 15. Effective slope parameters of transverse-momentum spectra of EM radiation in URHICs. Left panel: time dependence of $T_{\rm eff}$ of thermal photons, Eq. (16), in an expanding fireball for 0–20% central Au–Au ($\sqrt{s}$ = 200 AGeV) collisions at RHIC (solid blue line), compared to the local temperature (dashed line) and PHENIX data [55] (horizontal solid line with dashed-line error band); the dash-dotted line indicated the flow velocity of the fireball surface. Right panel: $T_{\rm eff}$ for excess dimuons as a function of their invariant mass as measured by NA60 in In–In ($\sqrt{s} = 17.3$ AGeV) collisions at SPS [38], compared to theory calculations [47] with different transverse fireball accelerations (lower 2 curves: $a_t = 0.085\,{\rm fm}/c^2$, upper 2 curves: $a_t = 0.1\,{\rm fm}/c^2$) and with different phase-transition temperatures (EoS-B: $T_{\rm c} = 160$ MeV, EoS-C: $T_{\rm c} = 190$ MeV).

prominently figures around $M \simeq m_\rho$; (b) the interplay of thermal factor and 3-volume implies that going up in mass the emission is "biased" toward the earlier phases (recall Fig. 10), which increases T but more strongly decreases the Doppler shift in Eq. (17), $M\langle\beta\rangle^2$; (c) for temperatures around $T_{\rm c}$ the duality of the emission rates renders a "partonic" and "hadronic" assignment ambiguous, depending on the not-so-well defined transition temperature. The latter is demonstrated by the two pair of lines in Fig. 15, where each pair is calculated assuming two "extreme" values of $T_{\rm c} = 160$ and 190 MeV. In the former case, the total thermal yield for masses M = 1–1.5 GeV is indeed dominated by QGP emission, while in the latter case hadronic emission prevails (with chiral mixing, *cf.* Fig. 6). The corresponding two curves in a pair essentially overlap. A more significant effect is due to transverse flow. The original predictions of fireball [57,58] and hydrodynamic [59] evolutions agree with each other, but underestimate the data [60] (*cf.* the lower pair of curves in Fig. 15, right). When implementing a stronger transverse expansion [47], comparable to that used at RHIC ($a_t = 0.1$ fm/c^2), a reasonable description of the NA60 slopes can be obtained (upper two curves in Fig. 15, right). Using the schematic slope formula with $T = 175$ MeV and an average QGP+mixed phase evolution time of 3 fm/c for semicentral In–In (resulting in $\langle\beta\rangle \simeq \frac{2}{3}a_t\tau = 0.2c$) gives an inverse slope of $T_{\rm eff} \simeq 215$ MeV

for $M \simeq 1\,\mathrm{GeV}$, as seen in the figure. The main point is that the NA60 slopes for $M \geq 1\,\mathrm{GeV}$ give an independent confirmation of thermal emission from a QCD medium with dual rate and temperature of around T_c. The sensitivity to the unexpectedly large collective flow shows that dileptons can also serve as an accurate "barometer" of the fireball. A similar analysis at RHIC should lead to much increased slope parameters, since the QGP has built up much more flow by the time it has cooled down to T_c. For example, from the left panel of Fig. 15 one finds $\beta_s \simeq 0.6\mathrm{fm}/c^2$ at the end of the mixed phase, translating into $T_\mathrm{eff} \simeq 350\,\mathrm{MeV}$ at $M \simeq 1$–$1.2\,\mathrm{GeV}$, see also Refs. [61, 62]. Finally, we remark that invariant-mass (rather than transverse-momentum) dilepton spectra can, in principle, provide a cleaner measurement of the temperature since it is Doppler-free. Of course, the richer (dynamic) structure in the low-mass regime complicates this task, but with a reliable knowledge of the in-medium spectral shape it is still possible; for the structureless regime above $M = 1\,\mathrm{GeV}$ the situation is even better. Analyzing the invariant-mass slopes of the NA60 spectra one finds temperatures ranging from 150–180 MeV for $M \simeq 0.2$–$1.5\,\mathrm{GeV}$, approaching 200 MeV for $M \geq 2\,\mathrm{GeV}$. The latter regime requires a good knowledge of the primordial contribution, *i.e.*, Drell–Yan annihilation and its nuclear corrections [63].

4. Conclusions

Electromagnetic emission spectra provide a rich observable to investigate the strongly interacting medium produced in high-energy collisions of heavy nuclei. The starting point for exploiting this observable is a thorough understanding of the vector spectral function in equilibrium matter. Chiral effective models at low and intermediate temperature and densities, lattice-QCD in the vicinity of the phase transition(s) and perturbative QCD in the high-temperature limit are starting to fill the theoretical landscape. The evidence is mounting for a melting of the hadronic vector-meson resonances and a transition to a partonic-like rate over the entire mass range. This, in particular, includes a large low-mass enhancement which is corroborated by recent lattice QCD results for Euclidean correlators and has been consistently showing in dilepton measurements from BEVALAC/SIS via SPS to RHIC. The state-of-the art in dilepton experimentation has been set by the NA60 dimuon results, which accurately confirm the resonance melting and show that it occurs right around the temperatures where lQCD predicts the chiral phase transition. This sets the stage for exciting developments to come, at both collider energies (RHIC and LHC, where the connections to lQCD are even more direct) and at lower energies as planned at the Compressed Baryonic Matter experiment (CBM, where the baryon-

induced medium effects are expected to become maximal). Several theoretical developments will have to accompany these efforts, including hadronic calculations of the axialvector to tighten the grip on chiral restoration using sum rules, lattice calculations of Euclidean correlators with dynamical quarks, and the implementation of equilibrium rates into state-of-the-art hydrodynamic models (possibly supplemented with transport simulations) which quantitatively describe bulk-hadron observables. One can thus hope that the systematic use of EM probes will continue to deliver unique and precise information on the phase structure of a strongly coupled nonabelian gauge theory.

I thank H. van Hees, C. Gale and J. Wambach for longterm fruitful collaboration on the presented topics, and Z. Fodor, L. McLerran, R. Pisarski and C. Ratti for interesting discussion. I am indebted to H.T. Ding, A. Francis and O. Kaczmarek for providing their newest lattice results. This work is supported by the US National Science Foundation under grant no. PHY-0969394 and by the A. v. Humboldt Foundation.

REFERENCES

[1] P. Braun-Munzinger, K. Redlich, J. Stachel, in: *Quark Gluon Plasma 3*, eds. R.C. Hwa, X.-N. Wang, World Scientific Publishing (2003) p. 491 [arXiv:nucl-th/0304013v1].

[2] K. Nakamura *et al.* [Particle Data Group], *J. Phys. G* **37**, 075021 (2010).

[3] T. Hirano, *Acta Phys. Pol. B* **42**, 2811 (2011), this issue.

[4] R. Rapp, J. Wambach, H. van Hees, in: *Relativistic Heavy Ion Physics*, ed. R. Stock, Landolt Börnstein New Series, Springer, 2010 [arXiv:0901.3289v1 [hep-ph]].

[5] C. Gale, in: *Relativistic Heavy Ion Physics*, ed. R. Stock, Landolt Börnstein New Series, Springer, (2010) [arXiv:0904.2184 [hep-ph]].

[6] F. Karsch, K. Redlich, A. Tawfik, *Eur. Phys. J.* **C29**, 549 (2003).

[7] S. Borsanyi *et al.* [Wuppertal–Budapest Collaboration], *J. High Energy Phys.* **1009**, 073 (2010).

[8] Z. Fodor and C. Ratti, private communication (2011).

[9] L. McLerran, R.D. Pisarski, *Nucl. Phys.* **A796**, 83 (2007); T. Kojo *et al.*, [arXiv:1107.2124 [hep-ph]].

[10] R. Rapp, *J. Phys. G* **31**, S217 (2005).

[11] S. Weinberg, *Phys. Rev. Lett.* **18**, 507 (1967).

[12] T. Das, V.S. Mathur, S. Okubo, *Phys. Rev. Lett.* **19**, 859 (1967).

[13] R. Barate *et al.* [ALEPH Collaboration], *Eur. Phys. J.* **C4**, 409 (1998).

[14] K. Ackerstaff *et al.* [OPAL Collaboration], *Eur. Phys. J.* **C7**, 571 (1999).
[15] R. Rapp, J. Wambach, *Adv. Nucl. Phys.* **25**, 1 (2000).
[16] J. Alam *et al.*, *Ann. Phys.* **286**, 159 (2001).
[17] S. Leupold, V. Metag, U. Mosel, *Int. J. Mod. Phys.* **E19**, 147 (2010).
[18] R. Rapp *et al.*, *Lect. Notes Phys.* **814**, 335 (2011).
[19] M. Urban *et al.*, *Nucl. Phys.* **A641**, 433 (1998).
[20] R. Rapp *et al.*, *Phys. Lett.* **B417**, 1 (1998).
[21] R. Rapp, C. Gale, *Phys. Rev.* **C60**, 024903 (1999).
[22] M. Dey, V.L. Eletsky, B.L. Ioffe, *Phys. Lett.* **B252**, 620 (1990).
[23] B. Krippa, *Phys. Lett.* **B427**, 13 (1998).
[24] G. Chanfray, J. Delorme, M. Ericson, M. Rosa-Clot, *Phys. Lett.* **B455**, 39 (1999).
[25] E. Braaten, R.D. Pisarski, T.C. Yuan, *Phys. Rev. Lett.* **64**, 2242 (1990).
[26] G. Aarts *et al.*, *Phys. Rev. Lett.* **99**, 022002 (2007).
[27] H.T. Ding *et al.*, *Phys. Rev.* **D83**, 034504 (2011).
[28] M. Asakawa, T. Hatsuda, Y. Nakahara, *Prog. Part. Nucl. Phys.* **46**, 459 (2001).
[29] R. Rapp, J. Wambach, *Eur. Phys. J.* **A6**, 415 (1999).
[30] C. Greiner, N. Haque, M.G. Mustafa, M.H. Thoma, *Phys. Rev.* **C83**, 014908 (2011).
[31] S. Turbide, R. Rapp, C. Gale, *Phys. Rev.* **C69**, 014903 (2004).
[32] J.I.Kapusta, P. Lichard, D. Seibert, *Phys. Rev.* **D44**, 2774 (1991).
[33] P.B. Arnold, G.D. Moore, L.G. Yaffe, *J. High Energy Phys.* **0112**, 009 (2001).
[34] G. Agakichiev *et al.* [CERES/NA45 Collaboration], *Eur. Phys. J.* **C41**, 475 (2005).
[35] D. Adamova *et al.* [CERES/NA45 Collaboration], *Phys. Rev. Lett.* **91**, 042301 (2003).
[36] R. Arnaldi *et al.* [NA60 Collaboration], *Phys. Rev. Lett.* **96**, 162302 (2006).
[37] D. Adamova *et al.* [CERES/NA45 Collaboration], *Phys. Lett.* **B666**, 425 (2008).
[38] R. Arnaldi *et al.* [NA60 Collaboration], *Eur. Phys. J.* **C59**, 607 (2009); **C61**, 711 (2009).
[39] S. Damjanovic, R. Shahoyan, H.J. Specht [NA60 Collaboration], *CERN Cour.* **49N9**, 31 (2009).
[40] A. Adare *et al.* [PHENIX Collaboration], *Phys. Rev.* **C81**, 034911 (2010).
[41] J. Zhao [STAR Collaboration], `arXiv:1106.6146v1 [nucl-ex]`.
[42] R.J. Porter *et al.* [DLS Collaboration], *Phys. Rev. Lett.* **79**, 1229 (1997).
[43] G. Agakishiev *et al.* [HADES Collaboration], *Phys. Lett.* **B663**, 43 (2008).

[44] I. Tserruya, in: *Relativistic Heavy Ion Physics*, ed. R. Stock, Landolt Börnstein New Series, Springer, 2010 [arXiv:0903.0415 [nucl-ex]].
[45] H.J. Specht [NA60 Collaboration], *AIP Conf. Proc.* **1322**, 1 (2010).
[46] R. Rapp, *Phys. Rev.* **C66**, 017901 (2002).
[47] H. van Hees, R. Rapp, *Nucl. Phys.* **A806**, 339 (2008).
[48] R. Rapp, *Phys. Rev.* **C63**, 054907 (2001).
[49] M.M. Aggarwal *et al.* [WA98 Collaboration], arXiv:1108.5400v1 [nucl-ex].
[50] A. Adare *et al.* [PHENIX Collaboration], *Phys. Rev. Lett.* **104**, 132301 (2010).
[51] R. Chatterjee, E.S. Frodermann, U.W. Heinz, D.K. Srivastava, *Phys. Rev. Lett.* **96**, 202302 (2006).
[52] F.M. Liu, T. Hirano, K. Werner, Y. Zhu, *Phys. Rev.* **C80**, 034905 (2009).
[53] H. Holopainen, S. Räsänen, K.J. Eskola, arXiv:1104.5371v1 [hep-ph].
[54] M. Dion *et al.*, arXiv:1109.4405v3 [hep-ph].
[55] A. Adare *et al.* [PHENIX Collaboration], arXiv:1105.4126v2 [nucl-ex].
[56] H. van Hees, C. Gale, R. Rapp, *Phys. Rev.* **C84**, 054906 (2011).
[57] H. van Hees, R. Rapp, *Phys. Rev. Lett.* **97**, 102301 (2006).
[58] J. Ruppert *et al.*, *Phys. Rev. Lett.* **100**, 162301 (2008).
[59] K. Dusling, D. Teaney, I. Zahed, *Phys. Rev.* **C75**, 024908 (2007).
[60] S. Damjanovic *et al.* [NA60 Collaboration], *Nucl. Phys.* **A783**, 327 (2007).
[61] J. Deng, Q. Wang, N. Xu, P. Zhuang, *Phys. Lett.* **B701**, 581 (2011).
[62] S. Ghosh, S. Sarkar, J.-e Alam, *Eur. Phys. J.* **C71**, 1760 (2011).
[63] J. Qiu, X. Zhang, *Phys. Lett.* **B525**, 265 (2002).